Comput Mech (2009) 44:455–471
DOI 10.1007/s00466-009-0383-6

ORIGINAL PAPER

Simulating the pervasive fracture of materials and structures using randomly close packed Voronoi tessellations

Joseph E. Bishop

Received: 20 December 2007 / Accepted: 25 February 2009 / Published online: 24 March 2009

Abstract Under extreme loading conditions most often the extent of material and structural fracture is pervasive in the sense that a multitude of cracks are nucleating, propagating in arbitrary directions, coalescing, and branching. Pervasive fracture is a highly nonlinear process involving complex material constitutive behavior, material softening, localization, surface generation, and ubiquitous contact. A pure Lagrangian computational method based on randomly close packed Voronoi tessellations is proposed as a rational and robust approach for simulating the pervasive fracture of materials and structures. Each Voronoi cell is formulated as a finite element using the Reproducing Kernel Method. Fracture surfaces are allowed to nucleate only at the intercell faces, and cohesive tractions are dynamically inserted. The randomly seeded Voronoi cells provide a regularized random network for representing fracture surfaces. Example problems are used to demonstrate the proposed numerical method. The primary numerical challenge for this class of problems is the demonstration of model objectivity and, in particular, the identification and demonstration of a measure of convergence for engineering quantities of interest.

Keywords Voronoi · Finite element · Fracture · Fragmentation · Cohesive crack · Sensitivity to initial conditions · Probabilistic

Sandia is a multi-program laboratory operated by Sandia Corporation, a Lockheed Martin Company, for the United States Department of Energy's National Nuclear Security Administration under Contract DE-AC04-94AL85000.

J. E. Bishop (✉)
Engineering Sciences Center, Sandia National Laboratories, Albuquerque, NM 87185, USA
e-mail: jebisho@sandia.gov

1 Introduction

Possible structural responses from extreme loading conditions, such as blast loads and impact, can range from intact vibrational response to complete fragmentation. A structure transitions from an intact continuum to a discontinuum through crack initiation and propagation. The extent of fracturing is termed pervasive when a multitude of cracks arbitrarily nucleate, propagate, coalesce, and branch. The simulation of pervasive structural fracture is further complicated by the ubiquitous self contact that accompanies new crack surfaces. In order to design structures to withstand extreme loading conditions it is imperative to have accurate computational methods for simulating pervasive failure. Any computational method that strives to model pervasive fracture must include the ability to numerically represent the progression of a body from a continuum description to a discontinuum description. In addition any computational method must be objective such that the simulation results do not depend on subjective properties of the model such as mesh design. One necessary condition for simulation objectivity is that the numerical approximation converges with discretization refinement. Without convergence to the necessary "engineering accuracy," numerical results and predictions are suspect, rendering validation, uncertainty quantification efforts, and general use in engineering design suspect as well.

Currently, there is a very limited set of computational tools available that can attempt to simulate the pervasive fracture of structures. Common and often unsatisfactory techniques include 'element death' in Lagrangian finite element codes and 'void insertion' in hydrocodes. The enriched finite element methods (Generalized Finite Element Method and Extended Finite Element Method) have had success in modeling dilute fracture problems [5,57]. Once crack branching and crack coalescence phenomena appear, the prospect of

modeling a multitude of arbitrary three-dimensional intersecting cracks quickly becomes untenable. However, great progress in this area has been obtained by Ghosh and coworkers [22,27,36,37] in the development of the Voronoi Cell Finite Element Method (VCFEM) based on an assumed-stress hybrid finite element method. The VCFEM has been used extensively to model material microstructure and quasi-static fracture. A variety of meshless or particle methods have been developed in the past fifteen years with the goal of modeling extreme deformation of solids including pervasive failure [6]. Examples include spherical particle hydrodynamics [2], Element-Free Galerkin [7], Reproducing Kernel Method [39], cracked particles [50], Material Point Method [59], particle in element [47], and element to particle conversion [32]. An interesting recent development is that of peridynamics [55] which is based on a nonlocal reformulation of the governing equations that eliminates the use of a deformation gradient, thus expanding the function space of possible deformations.

Ortiz [13,44–46,52,53] has pursued the concept of using standard finite element methods for modeling pervasive failure, in particular, tetrahedral meshes, but with fracture surfaces allowed to nucleate and propagate only along the interelement faces. At the inception of material softening and the localization of damage, the mesh connectivity is modified to reflect the new surface and a cohesive traction with a softening behavior is dynamically inserted. This seemingly severe restriction of only allowing fracture surfaces to nucleate at interelement faces, as opposed to unrestricted methods modeling single crack growth, offers several advantages in the simulation of pervasive failure. In a continuum the intersection of multiple arbitrarily intersecting general crack surfaces can result in subdomains whose surface topology is illposed for further computation. The restriction of only allowing new surfaces to form at interelement faces provides a necessary regularization of the resulting domain and surface topologies. For example, variational methods for solving the governing equations of motion, e.g. the finite element method, require that the domain have a Lipschitz continuous boundary. Thus, as the original domain fractures and disassociates into subdomains, each subdomain needs to have a Lipschitz continuous boundary as well. Also, the resulting subdomains could be arbitrarily small making further computation impossible in an explicit-dynamics framework. The restriction of only allowing new surfaces to form at interelement faces provides apriori the constraint on minimum edge size and subsequent critical-time step necessary in an explicit dynamic numerical solution. Furthermore, the restriction of only allowing new surfaces to form at interelement faces results in a time varying domain whose volume is continuous in time. This is not the case in most particle methods whose continuum representation evolves into a collection of spheres. (The theoretical maximum packing for equi-sized spheres is only 74%.) This continuity of volume in time can be very important in confined problems such as penetration and reconsolidation.

Herein, the approach of Ortiz is adopted for modeling pervasive fracture. Fracture surfaces are allowed to nucleate and propagate only along interelement faces of a domain mesh. At the inception of material softening and localization the mesh connectivity is modified to reflect the new surface and a cohesive traction with a softening constitutive behavior is dynamically inserted. However, the use of a tetrahedral mesh, albeit unstructured, is potentially biased with respect to edge and face orientation which could lead to nonobjective numerical predictions. Herein, instead of using a tetrahedral mesh, a randomly close packed (RCP) Voronoi tessellation [64] of the domain is used. The RCP Voronoi tessellation provides a random face network for representing fracture surfaces. The polyhedral cells of the RCP Voronoi tessellation are formulated as finite elements using the Reproducing Kernel Method [39]. The resulting polyhedral elements have a number of desirable properties including convexity and relatively large included angles. Additionally, the Voronoi face network provides a convenient discrete structure for studying fracture surface topology and percolation like processes during impact and fragmentation. The main challenge is to demonstrate that this finite basis set for representing fracture surfaces is sufficiently large to enable the predictive simulation of pervasive fracture processes.

The primary objectives of this paper are (1) to propose the use of randomly close-packed Voronoi tessellations for simulating pervasive fracture and (2) to elucidate the difficulties in defining and demonstrating convergence for this class of problems. Initially, only two-dimensional examples are given. Future work will focus on three-dimensional examples and quantitative comparisons with experiments. This paper is organized as follows. The problem formulation is given in Sect. 2. The randomly close-packed Voronoi tessellation is described in Sect. 3. Section 4 discusses the polyhedral finite element formulation based on the Reproducing Kernel Method. Section 5 gives a description of the dynamic mesh connectivity algorithm and an overview of the self-contact algorithm. A two-dimensional example is given in Sect. 6. A discussion on sensitivity to initial conditions and transient chaos is given in Sect. 7. A summary is given in Sect. 8.

2 Problem formulation

Consider the motion of a body $\mathscr{B}$ with interior domain Ω and boundary Γ subjected to a body force $\mathbf{f}$ and applied tractions $\mathbf{t}$. A pure Lagrangian description of the motion of $\mathscr{B}$ is used. The initial or reference domain of the body is denoted by Ω_o with boundary Γ_o. In the reference configuration, the position vector of a material point is denoted by $\mathbf{X}$. In the

deformed configuration, the position of a material point is denoted by $\mathbf{x}$, and the displacement $\mathbf{u} = \mathbf{x} - \mathbf{X}$. In the numerical solution to follow, interpolation functions will be constructed directly on the reference configuration. Therefore, a *total* Lagrangian formulation of the governing equations is appropriate [8]. The conservation of linear momentum is given by [7]

$$\frac{\partial \mathbf{P}}{\partial \mathbf{X}} : \mathbf{I} + \rho_o \mathbf{f} = \rho_o \ddot{\mathbf{u}}, \tag{1}$$

where $\mathbf{P}$ is the first Piola-Kirchhoff stress tensor, $\mathbf{f}$ is the body force vector per unit mass, ρ_o is the reference density, and $\mathbf{I}$ is the identity tensor. The weak form of Eq. 1 is given by

$$\int_{\Omega_o} \rho_o \ddot{\mathbf{u}} \cdot \delta\mathbf{u} \, d\Omega_o = \int_{\Gamma_o} \mathbf{t}_o \cdot \delta\mathbf{u} \, d\Gamma_o + \int_{\Omega_o} \rho_o \mathbf{f} \cdot \delta\mathbf{u} \, d\Omega_o - \int_{\Omega_o} \rho_o \mathbf{P} : (\partial(\delta\mathbf{u})/\partial\mathbf{X}) \, d\Omega_o \tag{2}$$

where $\delta\mathbf{u}$ is a virtual displacement vector, and $\mathbf{t}_o$ is the traction vector per unit reference area. The displacement $\mathbf{u}$ and virtual displacement $\delta\mathbf{u}$ are members of the Sobolev function space of degree one [8].

In the next section, a randomly close-packed Voronoi tessellation is used to mesh the reference domain Ω_o. The face network of the Voronoi mesh will be used as a random basis for representing new fracture surfaces in the deformed configuration. In Sect. 4, Eq. 2 will be solved using a Galerkin finite element approach where each Voronoi cell is formulated as a finite element directly on the reference configuration.

3 Randomly close-packed Voronoi tessellations

Voronoi tessellations have a rich history in mathematics and science and have a number of advantageous properties [43]. Given a finite set of points $\mathbf{X}_i$ or nuclei, the Voronoi tessellation is defined as the collection of regions or cells V_i where

$$V_i = \bigcap_{i \neq j} \{\mathbf{X} | d(\mathbf{X}_i, \mathbf{X}) < d(\mathbf{X}_j, \mathbf{X})\}. \tag{3}$$

Here, $\mathbf{X}$ represents an arbitrary point in the domain, and the function d is the Euclidean distance between two points. Each spatial point belonging to the Voronoi cell i is closer to nucleus i than all other nuclei. Note that each Voronoi cell is defined as the intersection of half-spaces and is thus convex. An example of a two dimensional Voronoi cell is shown in Fig. 1. While the Voronoi tessellation can be formed from any finite set of points or seeds, a special structure arises from the study of close packing of equi-sized hard spheres [1]. A classic experiment of dropping hard spheres into a relatively large container produces a structure known as random

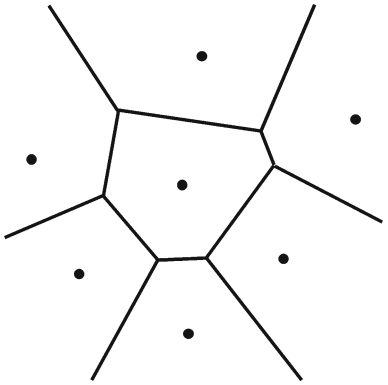

Fig. 1 A collection of points and their associated Voronoi diagram defined by Eq. 3

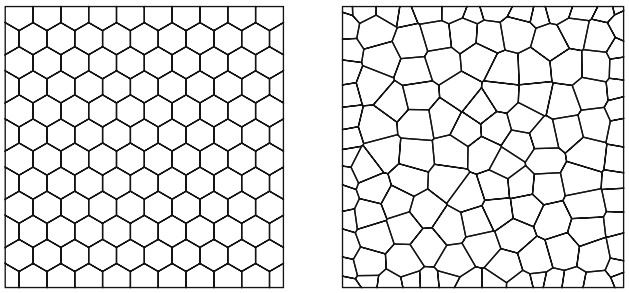

Fig. 2 The associated Voronoi diagram for both (**a**) an hexagonal close packed array of points, and (**b**) a randomly close packed array

close-packed (RCP) [64]. Unlike the well known hexagonal close-packed (HCP) structure with a packing factor of 0.740, the RCP structure exhibits a maximum packing factor of only 0.637. An example of the associated Voronoi tessellation for both the HCP and RCP structures in two dimensions is shown in Fig. 2. The RCP structure arises in a number of scientific fields and has been extensively studied. The RCP structure provides a foundation for the study of amorphous solids as described by Zallen [64]. The statistical geometry aspects of RCP structures and their associated Voronoi diagrams have been studied by Finney [20]. In three dimensions the average number of nearest neighbors is 14.3. For comparison, the number of nearest neighbors of the hexagonal close-packed structure is exactly 14. For the RCP structure the average aspect ratio of each Voronoi cell is approximately one. The median number of cell faces is 14 with a large majority of the face distribution in the range of 13 to 16. The median number of edges of each cell face is 5 with a large majority of the distribution in the 4 to 6 range. Most importantly each junction or node of the RCP Voronoi structure is randomly oriented with only a short range correlation to neighboring nodes. In two dimensions the RCP Voronoi structure results in cells with an average number of edges of exactly 6 and

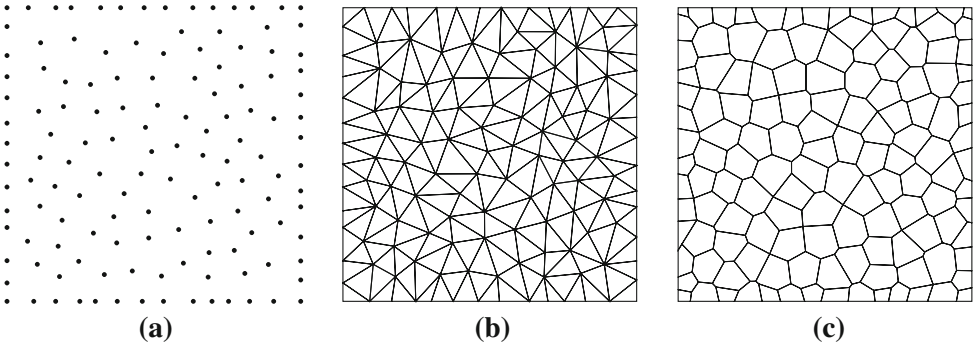

Fig. 3 Process used to create the randomly close packed Voronoi tessellation: (**a**) random seeding until the theoretical maximum packing is reached with a constraint on minimum distance between points, (**b**) Delaunay triangulation, and (**c**) dual Voronoi tessellation

an average interior vertex angle of approximately 120 deg [64]. These relatively large interior angles compared to conventional triangle and quadrilateral meshes are expected to result in relatively robust behavior in problems with large shear strains.

A common method for generating the RCP points is based on a variant of a homogeneous Poisson process and is known as random sequential adsorption or hard-core Gibbs process [40]. For a given characteristic length h, points are randomly and sequentially placed in the domain with a constraint on minimum distance between points. The constraint is enforced by merely discarding those new points that violate the constraint. The seeding process stops when the maximum packing threshold is reached within tolerance. Given the RCP point distribution, a number of techniques can be used to generate the Voronoi tessellation. Here, the domain is first triangulated using the Bowyer-Watson insertion algorithm resulting in a Delaunay triangulation (see Fig. 3) [12,61]. The Voronoi diagram is simply the dual of the Delaunay triangulation in the sense that the Voronoi cell nuclei are the vertices of the Delaunay triangulation, and the vertices of the Voronoi cells are the circumcenters of the Delaunay triangles. The generation of the Voronoi diagram is straight forward in unbounded domains but is nontrivial near geometrically 'complex' boundaries due to the need for intersection operations. Bolander [10,11,62,63] has used RCP Voronoi tessellations in spring-lattice models, and has developed a number of numerical techniques for handling nonconvex domains.

In practice the RCP Voronoi tessellation can contain a number of relatively small edges. These small edge lengths would cause an unacceptably small critical time-step in an explicit dynamics numerical solution. To regularize the mesh for use in explicit dynamics, any edge whose length is below a user specified tolerance is simply deleted and the attached nodes equivalenced. Figure 4 shows the effect of this mesh regularization step on the Voronoi tessellation given in Fig. 3. There is no discernable change in the tessellation. Histogram plots are also given showing the number of elements with a given number of edges both before and after the deletion of small edges. A majority of elements have six sides with all

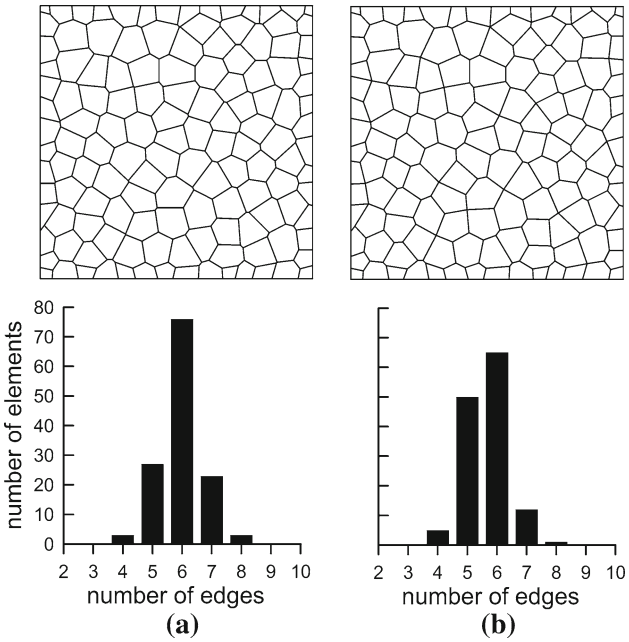

Fig. 4 Regularization of the Voronoi tessellation by removing relatively small edges and equivalencing nodes: (**a**) raw Voronoi tessellation and (**b**) Voronoi mesh with constraint on minimum edge size. The histogram of the number of elements for a given number of edges is also given

elements having in the range of four to eight sides after the small-edge regularization.

4 Finite element formulation

A general displacement based finite element formulation for plane faceted polyhedra applicable to large deformations has been achieved by Rashid [51] by developing incompatible polynomial based shape functions defined on the reference configuration that satisfy the minimum properties for convergence. Ghosh and coworkers [22,27,36,37] have extensively developed the Voronoi Cell Finite Element Method based on an assumed-stress hybrid finite element method. Idelsohn [31] used natural neighbor coordinates of a Delaunay tessellation of points to develop a "meshless" finite element method. Wachspress [60] used perspective geome-

try concepts to develop rational shape functions on polyhedra. Dai [18] has used the Smoothed Finite Element Method to develop Voronoi based finite elements. Sukumar [58] has developed a finite element formulation for convex polygons using shape functions defined on regular polygons. An alternative polyhedral finite element formulation is introduced here. The Reproducing Kernel Method [39] is used to generate compatible shape functions directly on the *original* configuration of the element. Thus, there is no mapping to a "parent" configuration. Without the need to map the polyhedron to a parent configuration, there is no apparent restriction on the shape of the element. In particular, non-convex elements are allowed.

4.1 Shape functions

Before applying the Reproducing Kernel Method [39] to the Voronoi mesh, the standard meshless development of the method is briefly reviewed. In the Reproducing Kernel Method, for a given node I, the shape function $\psi_I(\mathbf{X})$ is first generated by defining a nodal weight function $w_I(\mathbf{X})$ that (1) has compact support, (2) has a maximum value at the node, and (3) is smoothly and monotonically decreasing away from the node. In typical meshfree applications the nodal weight function is given a circular support in two dimensions and a spherical support in three dimensions. The nodal shape function is defined as a spatial modulation of the nodal weight function [6],

$$\psi_I(\mathbf{X}) = C_I(\mathbf{X}) w_I(\mathbf{X}) \tag{4}$$

where the nodal modulation function $C_I(\mathbf{X})$ is chosen so that $\psi_I(\mathbf{X})$ satisfies the desired reproducing and consistency requirements [6]. As described by Belytschko [6] a necessary condition for convergence is that the shape functions be able to at least reproduce polynomials through first order (linear consistency). Let $\mathbf{g}^{\mathrm{T}}(\mathbf{X})$ be the vector of desired scalar-valued basis functions, $g_i(\mathbf{X})$, $i = 1, 2, \ldots, n$

$$\mathbf{g}^{\mathrm{T}}(\mathbf{X}) = \{\, g_1(\mathbf{X})\ g_2(\mathbf{X})\ g_3(\mathbf{X})\ \ldots\ g_n(\mathbf{X}) \,\}. \tag{5}$$

For the special case of linear consistency only, the vector of basis functions $\mathbf{g}(\mathbf{X})$ is simply

$$\mathbf{g}^{\mathrm{T}}_{\mathrm{LC}}(\mathbf{X}) = \{\, 1\ X\ Y\ Z \,\}. \tag{6}$$

In general the basis could contain higher order polynomials or other "enrichment" functions. Let N be the set of all nodes whose weight function support contains the location $\mathbf{X}$. The reproducing property of the shape functions takes the form

$$\sum_{I \in N} \psi_I(\mathbf{X}) \mathbf{g}(\mathbf{X}_I) = \mathbf{g}(\mathbf{X}). \tag{7}$$

In order to satisfy Eq. 7, $C_I(\mathbf{X})$ is taken to be of the form

$$C_I(\mathbf{X}) = \mathbf{a}^{\mathrm{T}}(\mathbf{X}) g(\mathbf{X} - \mathbf{X}_I) \tag{8}$$

where

$$\mathbf{a}^{\mathrm{T}}(\mathbf{X}) = \{\, a_1(\mathbf{X})\ a_2(\mathbf{X})\ a_3(\mathbf{X})\ \ldots\ a_n(\mathbf{X}) \,\} \tag{9}$$

is a vector of unknown scalar valued functions, $a_i(\mathbf{X})$, $i = 1, 2, \ldots, n$.

For the present development only linear consistency is enforced. The restriction to linear consistency does not imply that the resulting shape functions are piecewise linear. In general the shape functions are rational functions [7]. Substituting Eqs. 8 and 6 into Eq. 7 yields, after some algebraic manipulation, the matrix equation

$$\mathbf{a}^{\mathrm{T}}(\mathbf{X}) = \{\, 1\ 0\ 0\ 0 \,\} \mathbf{A}^{-1}(\mathbf{X}) \tag{10}$$

where the 4×4 symmetric matrix $\mathbf{A}(\mathbf{X})$ is given by

$$\mathbf{A}(\mathbf{X}) = \sum_{J \in N} w_J(\mathbf{X} - \mathbf{X}_J) \mathbf{g}_{\mathrm{LC}}(\mathbf{X} - \mathbf{X}_J) \mathbf{g}^{\mathrm{T}}_{\mathrm{LC}}(\mathbf{X} - \mathbf{X}_J) \tag{11}$$

where $\mathbf{g}_{\mathrm{LC}}(\mathbf{X})$ is defined in Eq. 6. Calculation of the inverse of $\mathbf{A}(\mathbf{X})$ in Eq. 11 allows for the solution of $\mathbf{a}(\mathbf{X})$ in Eq. 10 and subsequently $C_I(\mathbf{X})$ in Eq. 8. By construction both the reference coordinate $\mathbf{X}$ and the displacement field $\mathbf{u}$ are interpolated by the shape functions $\psi_I(\mathbf{X})$

$$\mathbf{X} = \sum_{I \in N} \psi_I(\mathbf{X}) \mathbf{X}_I, \quad \mathbf{u} = \sum_{I \in N} \psi_I(\mathbf{X}) \mathbf{u}_I \tag{12}$$

where $\mathbf{X}_I$ and $\mathbf{u}_I$ are the nodal positions and displacements, respectively. Thus, by definition this element formulation is isoparametric. The spatial derivatives of the shape functions can be calculated by direct differentiation of Eqs. 8, 10, and 11 as described in [7].

Now consider the application of this general shape function construction to a Voronoi mesh of a domain Ω_{o} with boundary Γ_{o}. First, the nodal weight function w_I is defined as follows. The compact support of w_I is chosen to be the union of element domains attached to node I as with standard finite elements. Let this domain be denoted by Ω_I with boundary Γ_I and unit normal $\mathbf{n}$. The nodal weight function $w_I(\mathbf{X})$ is defined as the solution to the Poisson boundary value problem,

$$\begin{aligned} \nabla^2 w_I + 1 &= 0 \quad \text{in } \Omega_I \\ w_I &= 0 \quad \text{on } \Gamma_I \cap \Gamma_{\mathrm{o}} = \emptyset \\ \nabla w_I \cdot \mathbf{n} &= 0 \quad \text{on } \Gamma_I \cap \Gamma_{\mathrm{o}} \neq \emptyset. \end{aligned} \tag{13}$$

Given the nodal weight function w_I, Eqs. 4–11 can be used to calculate the nodal shape function ψ_I. It is important to note that by construction, for any two nodes I and J, $\psi_I(\mathbf{X}_J) = \delta_{IJ}$, so that the shape functions satisfy the Kronecker delta property as with standard finite elements. This property greatly simplifies the imposition of displacement boundary conditions, and is absent in the general use of the reproducing kernel method as a meshless method [6]. Figure 5 shows the

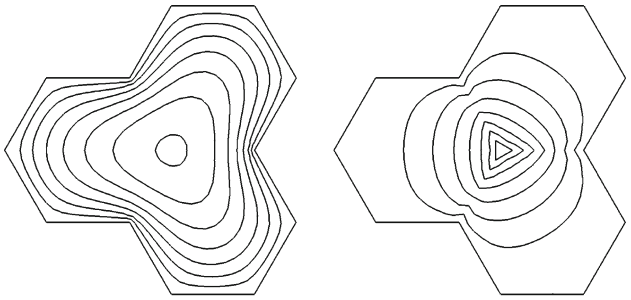

Fig. 5 **a** Contour plot of the nodal weight function for an interior node of a regular hexagonal mesh. The weight function is obtained by solving the local boundary value problem defined by Eq. 13. **b** Contour plot of the shape function resulting from the application of the Reproducing Kernel Method

weight function and resulting shape function corresponding to an interior node of a regular hexagonal mesh.

Since the value of the shape function and its partial derivatives are only needed at the Voronoi cell integration points, $\mathbf{X}_k, k = 1, \ldots, M$, the weight function and its partial derivatives need only be evaluated there as well. Since the solution to the Poisson problem Eq. 13 is needed only at a finite number of points, a boundary element solution method would be the most efficient [35]. However, in the two-dimensional example problem given in Sect. 6, a finite element method based on first-order triangles was used. Since a total Lagrangian formulation of the momentum equation is used, the shape functions and their derivatives only need to be calculated once at the beginning of the analysis and stored for later use.

4.2 Element integration

Rashid [51] has proposed a general method for developing Gauss points and their weights for integrating three-dimensional polyhedral elements. For the two-dimensional applications presented here, a reduced approach is adopted since each element domain is star shaped and can be triangulated by connecting the element nodes to the element centroid. Standard Gauss rules for triangles can then be applied. Additionally, Chen [16] has noted that the linear consistency enforced in the construction of the shape functions does not guarantee a linear exactness in the element formulation, i.e. satisfaction of the patch test. Fundamentally, this is due to a violation of the discrete form of Gauss' theorem and can result in a reduced accuracy and rate of convergence. For a given shape function ψ the continuous version of Gauss' theorem over an element subdomain Ω_e with boundary Γ_e and outward unit normal $n_i, i = 1, 2, 3$ is given by

$$\int_{\Omega_e} \psi_{,i}\, d\Omega_e = \int_{\Gamma_e} \psi n_i\, d\Gamma_e. \tag{14}$$

The discrete approximation resulting from numerical integration is then

$$\sum_k \omega_k \psi_{,i}^{\,k} \simeq \sum_k \omega_k^{\Gamma} \psi^k n_i^k \tag{15}$$

where $\psi^k \equiv \psi(\mathbf{X}_k)$ and $\mathbf{X}_k$ are the integration points with weights ω_k in the domain and ω_k^{Γ} on the element boundary. While Eq. 14 is a mathematical identity for any sufficiently smooth function, Eq. 15 does not hold in general. Herein, to maintain equality in Eq. 15 the shape function derivatives at the integration points are modified by solving a least squares problem of the difference of the shape function derivatives and their original values with equality in Eq. 15 imposed as a constraint:

$$\min_{a^{ik} \in \Re} \sum_{k=1}^{M} \left(\psi_{,i}^{\,k} - a^{ik} \right)^2 \tag{16}$$

subject to the constraint

$$\sum_k \omega_k a^{ik} - \sum_k \omega_k^{\Gamma} \psi^k n_i^k = 0 \tag{17}$$

where a^{ik} is the modified shape function derivative at the kth integration point. The solution to Eqs. 16 and 17 was obtained using the method of Lagrange multipliers. Typical corrections in the shape function derivatives are a few percent. These corrections are local to each element and thus do not require a global equation solution. Since a total Lagrangian formulation of the momentum equation is used, the shape function derivatives are only corrected once at the start of the analysis.

4.3 Verification

For an element verification study, the boundary value problem of a cantilevered beam with an end load is used (see Fig. 6). The exact boundary conditions and solution in both plane stress and plane strain are given in Hughes [28]. For reproducibility a mesh of regular hexagons is used. The length to thickness ratio of the beam is fixed at 4.62. Figure 7 shows the effect of the shape function derivative correction on the L_2 norm of the displacement error as a function of cell size, h. The L_2 convergence rate is only 1.13 without the correction, but 1.88 with the correction. Figure 8 shows the sensitivity of the L_2 norm of the displacement error to random spatial perturbations in the regular hexagonal mesh. The normalized maximum perturbation for each mesh is denoted by r. There is only a small sensitivity to the initial shape of the elements.

To handle near incompressibility, a standard mean dilation formulation is used [29,51]. Figure 9 shows the effect of Poisson's ratio, ν, on the L_2 norm of the displacement error for the case of plane strain. The mean dilation formulation effectively eliminates the typical locking behavior. Figure 10

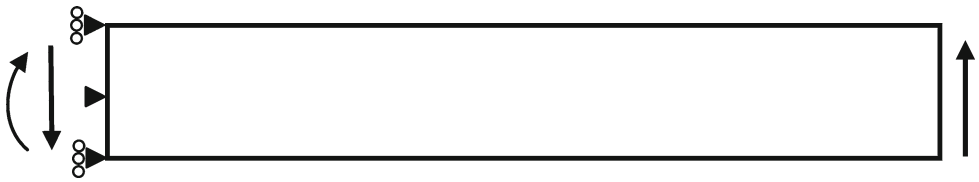

Fig. 6 Beam-bending element verification problem (plane stress or plane strain, length to thickness ratio is 4.62)

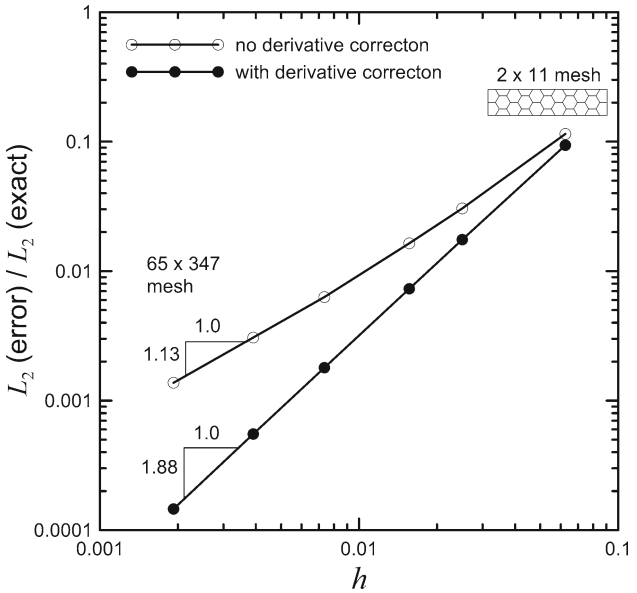

Fig. 7 Effect of integration consistency on the L_2 norm of the displacement error for the beam-bending verification problem using a regular hexagonal mesh with cell size, h (plane stress, Poissons ratio = 0.3, three integration points per element vertex)

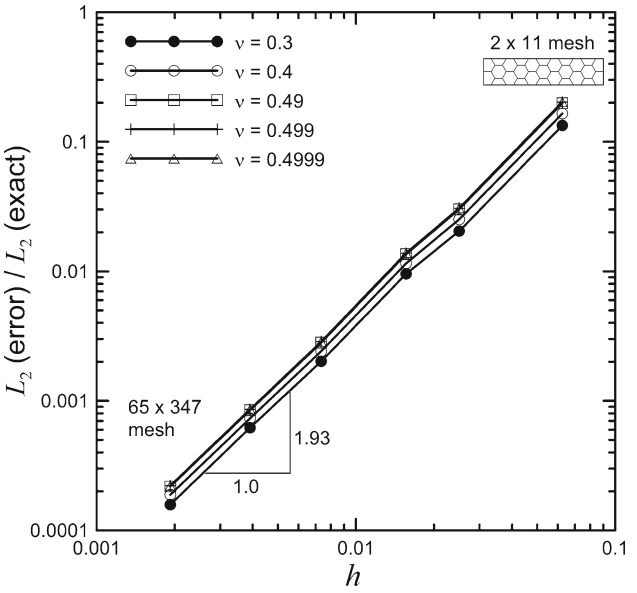

Fig. 9 Effect of Poissons ratio, ν, on the L_2 norm of the displacement error for the beam-bending verification problem using a mean dilation formulation (plane strain, three integration points per element vertex, $r = 0.2$)

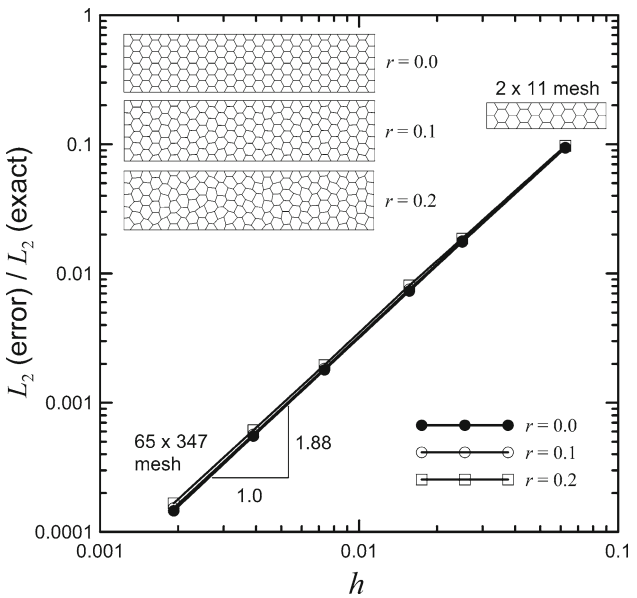

Fig. 8 Sensitivity of the L_2 norm of the displacement error to random perturbations in the regular hexagonal mesh for the beam-bending verification problem (plane stress, Poissons ratio = 0.3, three integration points per element vertex). The normalized maximum perturbation for each mesh is given by r

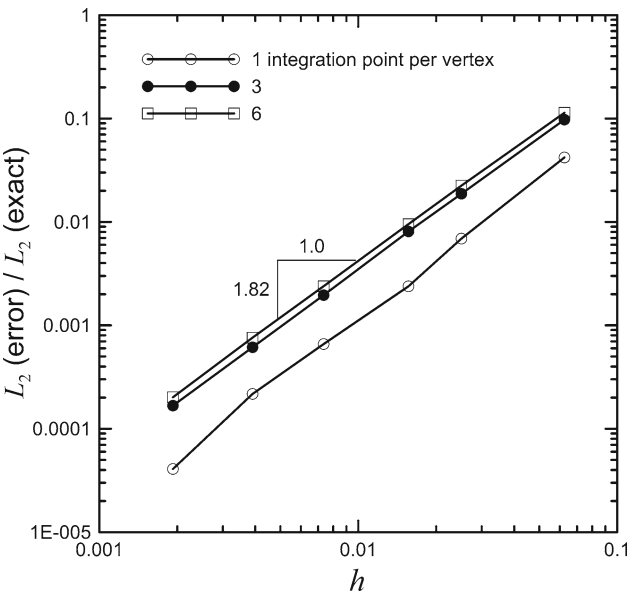

Fig. 10 Effect of number of element integration points on the L_2 norm of the displacement error for the beam-bending verification problem (plane stress, Poissons ratio = 0.3, $r = 0.2$)

shows the effect of the number of integration points per element vertex on the L_2 norm of the displacement error for the case of plane stress. The use of one integration point per vertex results in increased accuracy for the plane stress case while avoiding zero-energy modes. Conversely, for the plane strain case (not shown) an opposite trend was observed.

4.4 Time integration

To numerically integrate Eq. 2 in time, a typical explicit-dynamics central difference time integration scheme is used [9]. To obtain a diagonalized mass matrix, the "special lumping technique" of Hinton [25] is used. This mass lumping procedure is recommended by Hughes for non-standard element formulations as it is guaranteed to produce positive lumped masses [30].

5 Dynamic mesh connectivity and contact

5.1 Dynamic mesh connectivity

The creation of one or more new fracture surfaces (faces in three dimensions and edges in two dimensions) can occur in each time step in a simulation. For crack initiation in the interior of the body, at least two cracked edges are needed to realize a change in the mesh connectivity in two dimensions. In three dimensions at least three faces are needed. For crack initiation on the boundary of a body, only one cracked edge is needed to realize a change in the mesh connectivity in two dimensions, while in three dimensions at least two faces are needed. To facilitate this change in mesh connectivity during the simulation, an efficient algorithm and data structure is needed that is also simple and free of special cases. Pandolfi [46] has presented a general algorithm and data structure for tetrahedral meshes. Herein, an algorithm based on equivalence classes is used. In abstract algebra an equivalence relation is a generalization of equality [21]. An equivalence relation on a set S is a set R of ordered pairs of elements of S such that (1) $(a, a) \in R$ for all $a \in S$, (2) $(a, b) \in R$ implies $(b, a) \in R$, and (3) $(a, b) \in R$ and $(b, c) \in R$ imply $(a, c) \in R$. If R is an equivalence relation on a set S, one can write more clearly aRb instead of $(a, b) \in R$. Let $\sim$ denote an equivalence relation on S and $a \in S$, then the set $[a] = \{x \in S | x \sim a\}$ is the equivalence class of S containing a. A partition of a set S is a collection of nonempty disjoint subsets of S whose union is S. The equivalence classes of an equivalence relation on a set S constitute a partition of S [21].

To simplify the algorithm discussion, consider the case of a two-dimensional mesh. (The three-dimensional algorithm is identical in structure.) Three types of programming objects are used: (1) element objects, (2) edge objects, and (3) global node objects. An element object consists of its vertices and a mapping to global nodes. This mapping to global nodes will change after a mesh connectivity update. An edge object consists of two attached elements (one of which may be null if the element is on the boundary) and four element vertices (two for each attached element). The node object consists of solution information such as position and velocity. If an edge object is *not* fractured then its set of four element vertices will map to only two unique global node objects. Let a_i represent the ith vertex of the ath element. Let S be a set of element vertices. The equivalence relation $\sim$ is defined such that $a_i \sim b_j$ if the two element vertices are part of an *uncracked* edge and each is from a different element. This equivalence relation may be used to partition any set of element vertices into equivalence classes. Each equivalence class may then be identified as a new global node. An example of this algorithm is given in Fig. 11, and is detailed below:

1. **Initialization**
   (a) Create an element work set, W, consisting of all elements connected to fractured edges.
   (b) Create an edge object work set, W_e, consisting of all edge objects whose attached elements are in W.
   (c) Let S the set of all element vertices of W; $S = \{a_1, \ldots, a_n, b_1, \ldots, b_m, \ldots\}$
   (d) Initialize the partition P of S by taking each element vertex to be a set; $P_{\text{init}} = \{\{a_1\}, \ldots, \{a_n\}, \{b_1\}, \ldots, \{b_m\}, \ldots\}$
2. **Partition** Loop over all edge objects in W_e.
   (a) if fractured then equivalence element vertices attached to this edge object by uniting sets in P.
3. Each item in P is now an equivalence class. Create a global node object for each equivalence class.
4. Transfer nodal data (e.g. position, velocity) from old global nodes to new global nodes.

Note that the partition step requires only a single pass through the set of edges in the edge work set W_e.

5.2 Contact

Pervasive fracture involves a large amount of self-contact between new fracture surfaces. It is essential to have a simple and robust contact algorithm that can handle large sliding and changes in surface topologies. To avoid any constraints on surface topology that is typical of master/slave contact algorithms, a simple penalty approach is adopted here. Each polyhedral element is treated independently and checked for mutual penetration as in the discrete element method [41]. Only those elements that are on the initial boundary

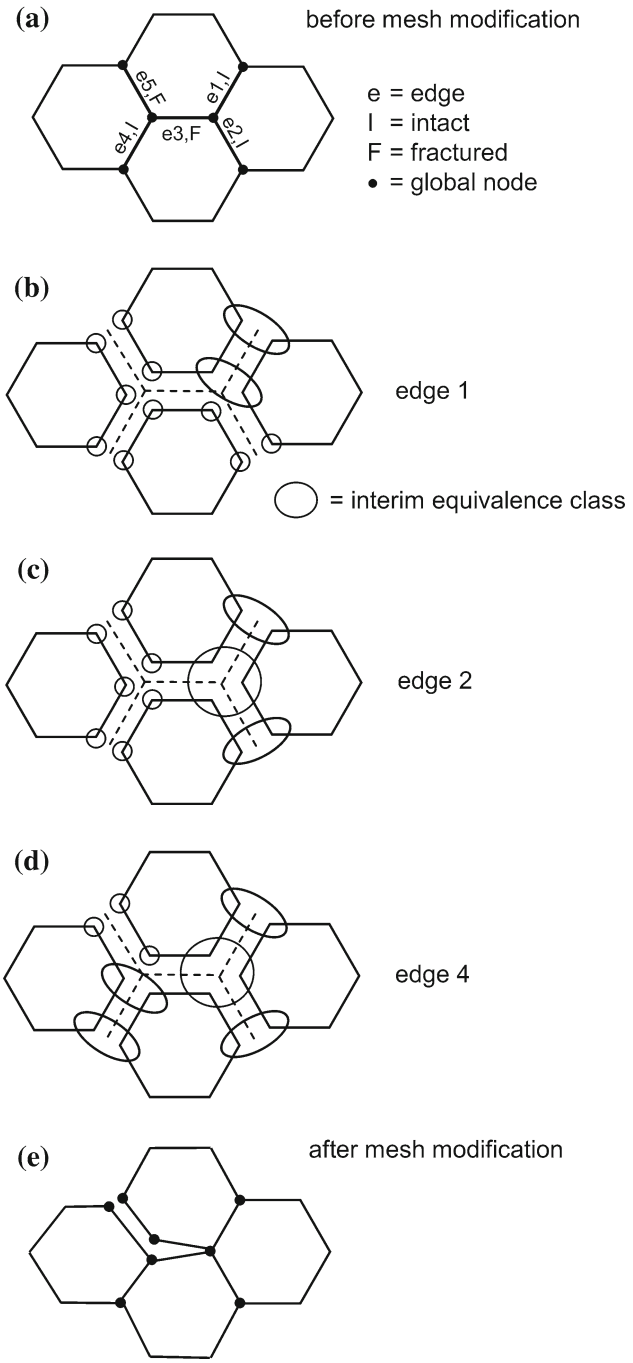

Fig. 11 Example of the dynamic mesh connectivity algorithm: (**a**) a four element submesh with two edges marked as fractured and three edges marked as intact; global nodes are shown with solid circles, (**b**) fully disconnected mesh with edge connectivities shown with dashed lines; interim equivalence classes are shown with open circles/ellipses; intact state of edge 1 is used to unite interim equivalence classes, (**c**) intact state of edge 2 is used to unite interim equivalence classes, (**d**) intact state of edge 4 is used to unite interim equivalence classes, (**e**) after all intact edges have been visited, final equivalence classes become new global nodes

of the domain or have a fractured face need to be considered for contact. If penetration is detected, a penalty force based on both the penetrating velocity and penetration is applied following Heinstein [24]. Due to the faceted nature of the polyhedral elements, surface normals are smoothed to prevent discontinuous sliding behavior.

6 Example

For an example with pervasive fracture that involves both initial impact fragmentation as well as late time structural fracture, consider a low-strength concrete column (0.3×1.83 m) impacting a rigid plane at a striking velocity of 7.6 m/s and 45° angle-of-attack as shown in Fig. 12. The column is idealized as a two-dimensional plane strain structure composed of a linear elastic material (Young's modulus $E = 28.3$ GPa, Poisson's ratio $\nu = 0.2$, density $\rho = 2.25$ g/cc) with a Mohr-Coulomb damage-localization criterion containing a tensile cutoff σ_o as shown in Fig. 13. The Mohr–Coulomb criterion is given by

$$|\tau| = c - \mu\sigma \tag{18}$$

where τ is the limiting shear stress on a plane, σ is the normal stress on the same plane, c is the cohesion, and μ is the coefficient of internal friction. For this example, $c = \sigma_o = 3.7$ MPa and $\mu = 0.75$. The cohesive traction model follows that of Camacho and Ortiz [13]. The cohesive parameters presented in reference [49] for mortar are used with an overall fracture energy $G = 57\,\mathrm{J/m^2}$. An estimate of the cohesive-zone length can be obtained using an equivalent linear elastic fracture mechanics model in which the length of the cohesive zone, L, is given by $L = kl_{ch}$, where $l_{ch} = E'G/\sigma_o^2$ is Hillerborg's characteristic size, $E' = E/(1-\nu^2)$, and k is a dimensionless constant in the range 2 to 5 [4,17]. Using the above material values gives $l_{ch} = 0.12$ m and a minimum value for L of 0.25 m. This value for the length of the cohesive zone is roughly equal to the thickness of the concrete column in the present example, and should be adequately resolved.

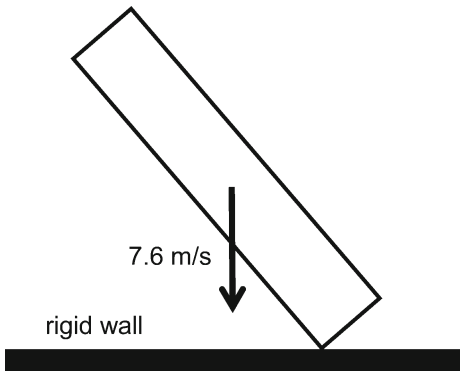

Fig. 12 A low-strength concrete column striking a rigid wall at a 45° degree angle

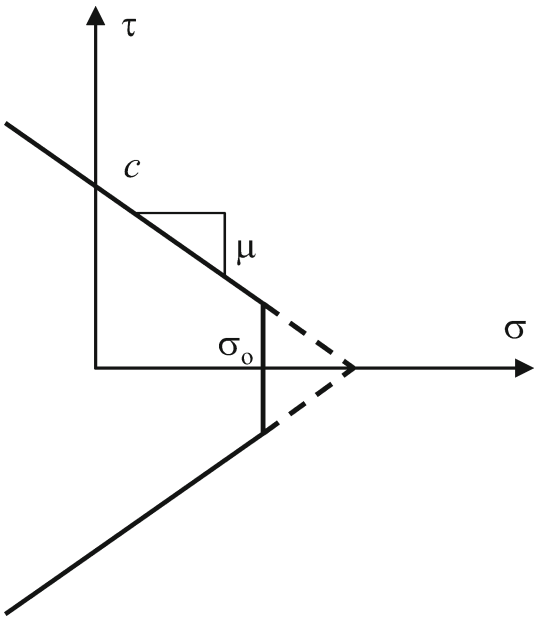

Fig. 13 Mohr-Coulomb failure surface in shear (τ)—normal (σ) stress space, with cohesion c, tensile cutoff σ_o, and internal friction μ

A two-dimensional explicit-dynamics program implementing the RCP Voronoi method of Sects. 3, 4, and 5 was developed using the C++ programming language. The Standard Template Library [33], providing the *set*, *vector*, *list*, and *map* dynamic data structures, was particularly useful. In order to detect if the localization criterion Eq. 18 has been met at an interelement face, the stress field is interpolated from the integration points of the two attached elements. Once the localization criterion is met at an interelement face, the connectivity of the finite element mesh is updated as described in Sect. 5.1, and the cohesive traction model is invoked. The normal tractions are taken to be zero under over-closure. The contact algorithm of Sect. 5.2 is used to prevent interelement penetration.

For the results and discussion to follow, the ith realization of a RCP Voronoi tessellation with a characteristic cell size h will be denoted by R_i^h. Four characteristic cell sizes will be considered, 8, 4, 2, and 1, with $h = 1$ corresponding to a physical dimension of 0.635 cm. Three realizations of the RCP Voronoi mesh are shown in Fig. 14 for $h = 8, h = 4$, and $h = 2$. Figure 15 shows a series of snapshots in time of the concrete column during the impact event using the R_1^2 mesh. In addition to the boundary, fracture surfaces whose cohesive tractions have fully softened are also shown. There is extensive fragmentation at the impact corner. Note the bending induced fracture at the midsection involving crack coalescence and branching. There is additional fragmentation after the column rotates and the rear section strikes the rigid plane at approximately 200 ms. The fragmentation process is essentially complete by 300 ms. Due to the ubiquitous contact and pervasive fracture present in this problem, the simulation results are expected to be extremely sensitive to initial conditions and system parameters. To illustrate the extreme sensitivity to initial conditions, the simulation was rerun using an identical RCP mesh but with an initial angle-of-attack of 44.99°, only a 0.02% change in initial conditions. The simulation results are shown in Fig. 16. Note that the fracture

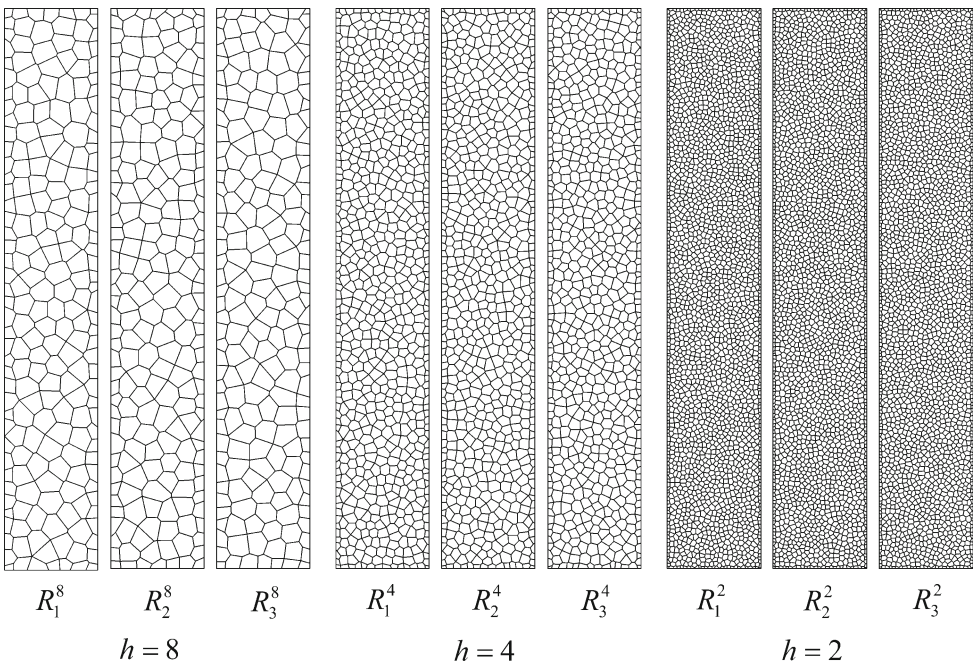

Fig. 14 Randomly close packed Voronoi realizations for three different characteristic cell sizes, $h = 8$, $h = 4$, and $h = 2$. Three realizations are shown for each characteristic cell size

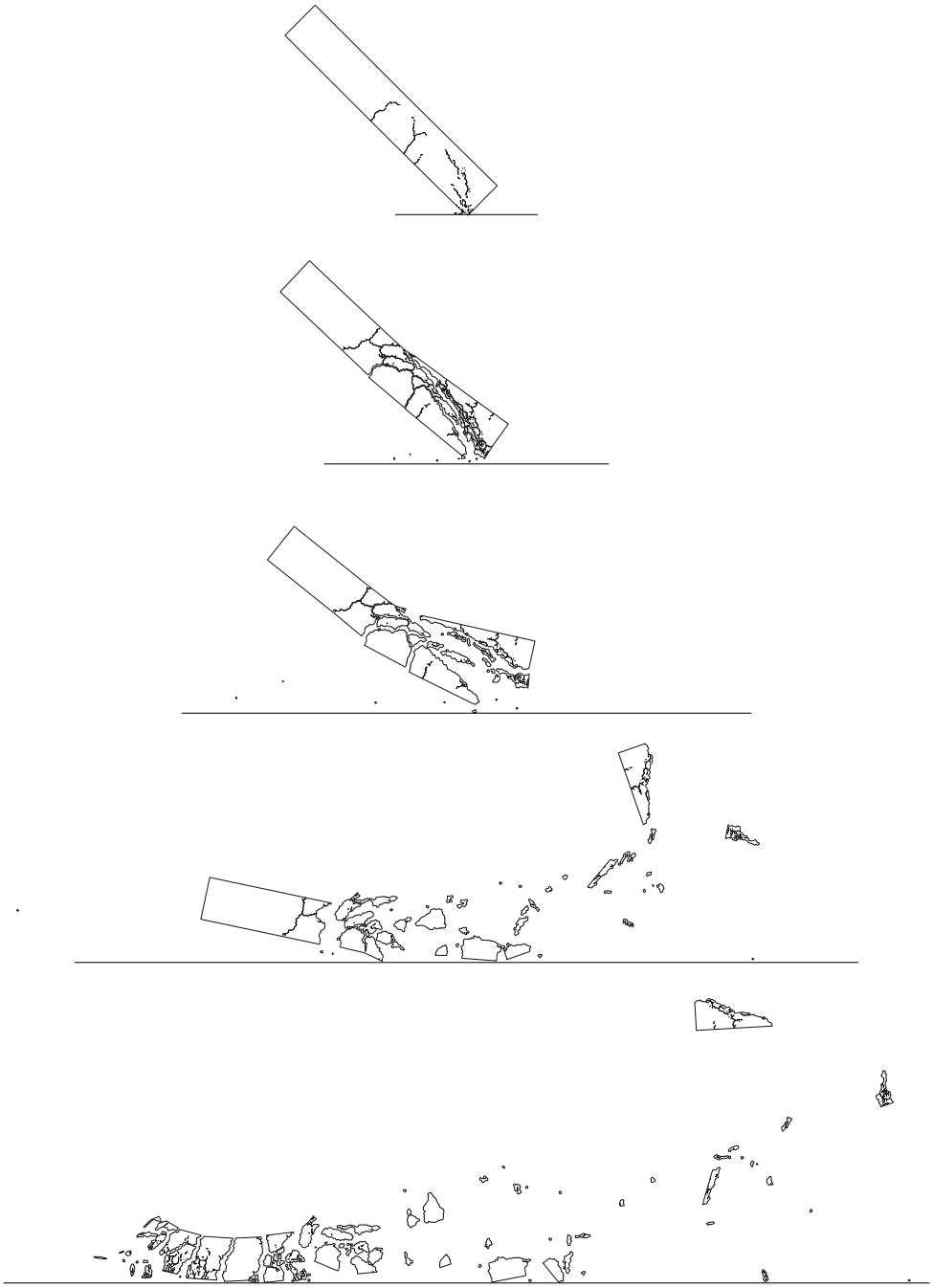

Fig. 15 Deformed state and crack surfaces of the concrete column at a number of instances in time after impact with an impact angle of 45.00° (R_1^2 mesh). Only cracks that have fully softened (no cohesive tractions) are shown. Impact times are 2, 10, 30, 150, and 230 ms

and fragmentation results are qualitatively similar but distinctly different with respect to specific cracks and resulting fragment sizes.

Since the concrete column is idealized as spatially homogenous in these simulations, the random orientation of the RCP Voronoi structure provides in effect a non-physically based variation in the localization properties of the material. Performing multiple simulations with different RCP Voronoi realizations will result in a distribution of results. (Of course, ideally, one would use correlated random fields to model the material properties including those used in the localization criterion, Eq. 18.) Suppose the engineering quantity of interest is the cumulative distribution of fragment mass-fraction, a common measure used in describing fragmentation results. The cumulative distribution at the simulation time of 300 ms is shown in Fig. 17 for twelve RCP Voronoi realizations of the R_i^8 mesh family. Note the large variation in results. The maximum fragment size for a given simulation may be identified by the last step in the curve.

The cumulative distributions in fragment mass-fraction for the R_i^4, R_i^2, and R_i^1 mesh families are shown in Figs. 18, 19, and 20, respectively. The convergence of the

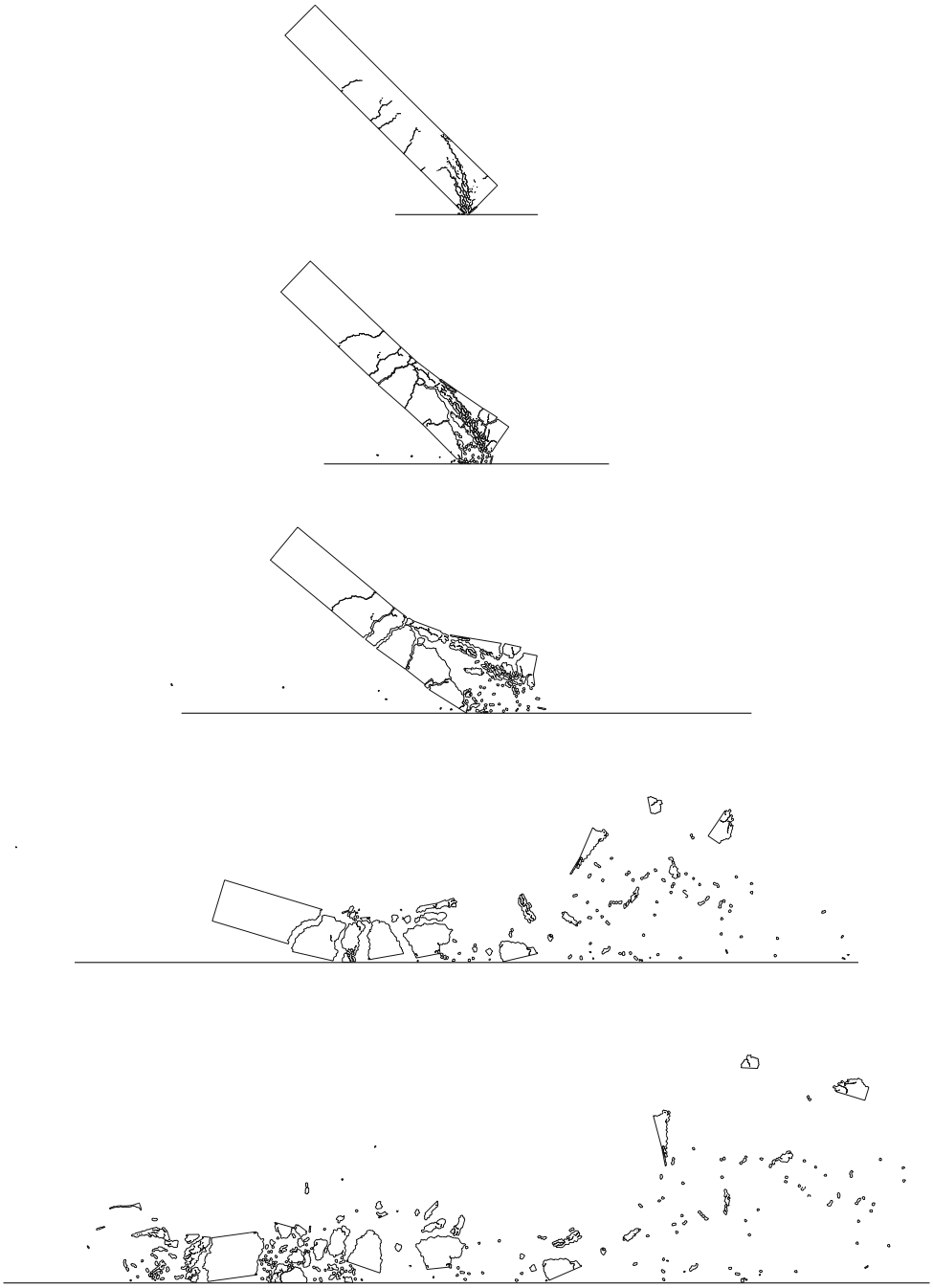

Fig. 16 Deformed state and crack surfaces of the concrete column at a number of instances in time after impact with an impact angle of 44.99° (R_1^2 mesh). Only cracks that have fully softened (no cohesive tractions) are shown. Impact times are 2, 10, 30, 150, and 230 ms

distribution of cumulative distributions with mesh refinement is not apparent, although twelve realizations is a very small sample size for what is expected to be a complex statistical distribution for fragment size. A definitive demonstration of convergence, if present, could necessitate thousands of such simulations. Such Monte Carlo analyses would be challenging for large scale three-dimensional problems.

The computational problem is further complicated by the fact that the use of interelement cohesive based finite element simulations is predicated on a mesh resolution that is finer than the cohesive zone size, which is certainly true for this example, but for many material systems such as brittle ceramics the cohesive zone size is relatively small and can be computationally expensive to resolve. Recently, Molinari [42] has performed a detailed investigation into the convergence behavior of the total dissipated cohesive energy for a fragmenting ceramic ring in a one dimensional setting using a random mesh. Extremely fine meshes were needed to demonstrate convergence in the mean value. Resolving a full probability distribution would be even more challenging.

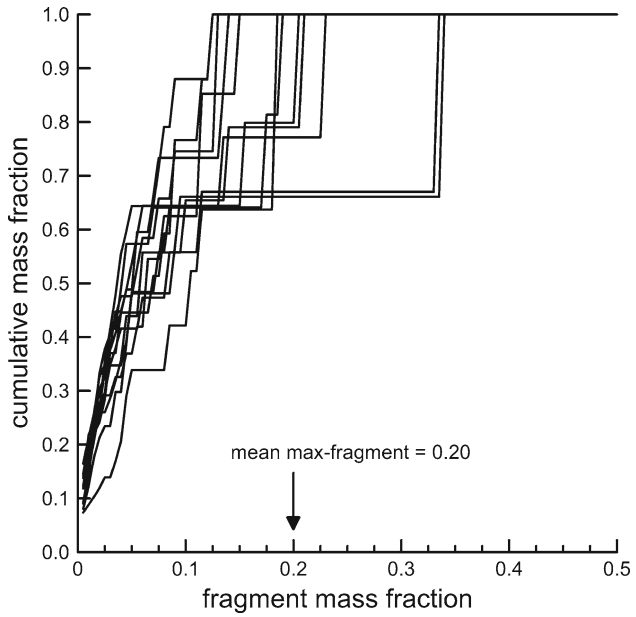

Fig. 17 Cumulative distribution of the fragment mass-fraction at a simulation time of 300 ms for the R_i^8, $i \in \{1, \ldots, 12\}$ RCP Voronoi mesh family. The mean of the maximum-fragment mass-fraction is denoted by the arrow

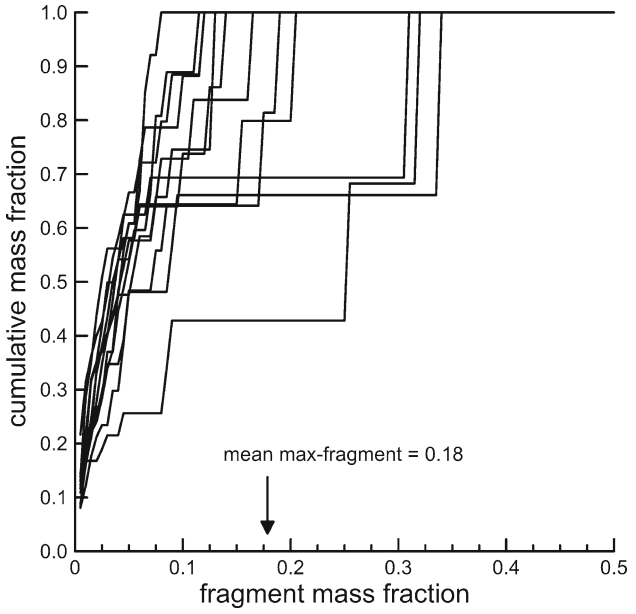

Fig. 19 Cumulative distribution of the fragment mass-fraction at a simulation time of 300 ms for the R_i^2, $i \in \{1, \ldots, 12\}$ RCP Voronoi mesh family. The mean of the maximum-fragment mass-fraction is denoted by the arrow

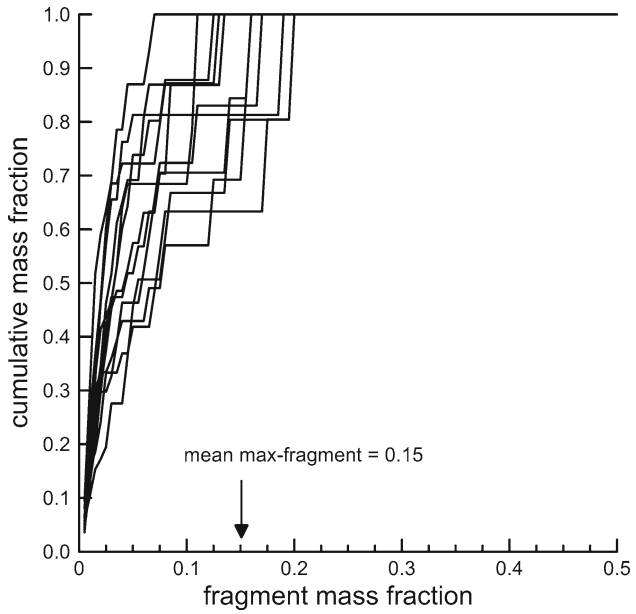

Fig. 18 Cumulative distribution of the fragment mass-fraction at a simulation time of 300 ms for the R_i^4, $i \in \{1, \ldots, 12\}$ RCP Voronoi mesh family. The mean of the maximum-fragment mass-fraction is denoted by the arrow

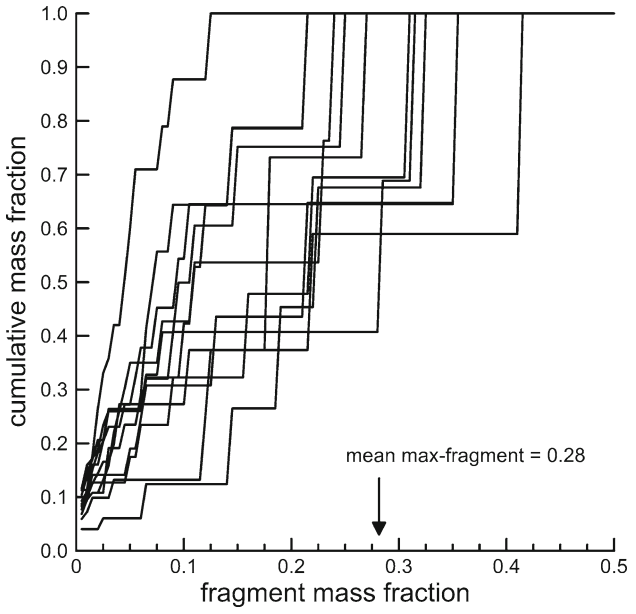

Fig. 20 Cumulative distribution of the fragment mass-fraction at a simulation time of 300 ms for the R_i^1, $i \in \{1, \ldots, 12\}$ RCP Voronoi mesh family. The mean of the maximum-fragment mass-fraction is denoted by the arrow

An additional consideration arises with the use of bulk constitutive models that include internal state variables for representing continuum damage from microcracking. The presented computational method provides an explicit representation of macroscopic cracks. Continuum damage mechanics provides an implicit homogenized representation of microcracks. As an RCP Voronoi mesh is refined to smaller scales the question of self-consistency between the explicit macroscopic representation of cracks and the implicit homogenized representation comes into question. This notion of

self-consistency and scale dependence is a central theme in fractal geometry descriptions of materials [14,15,26,48], and is important for understanding the size effect in quasi-brittle materials such as concrete [3,4].

7 Sensitivity to initial conditions

The previous example illustrates the challenge of defining and demonstrating a measure of convergence for the pervasive failure class of problems. Fundamentally, this difficulty arises due to extreme sensitivity in initial conditions and system parameters. The face network provided by the Voronoi tessellation provides a convenient discrete structure for studying this sensitivity.

7.1 Transient chaos

In the mathematical field of nonlinear dynamics it is now well known that there exist many deterministic systems that are inherently unpredictable beyond a certain critical time, the so called predictability horizon [54,56]. Such problems exhibit an exponential growth in time of small variations in the initial conditions and therefore possess an inherent predictability limit in time [56]. To see this let $x(t)$ represent a trajectory in phase space for a dynamical system. Let $x(t)+\delta(t)$ represent a slightly different trajectory in which the initial conditions are varied by a very small amount δ_o. The difference in the two trajectories $\delta(t)$ can be described by the relation

$$\|\delta(t)\| \sim \|\delta_o\| e^{\lambda t} \tag{19}$$

where λ is the Liapunov exponent. If λ is positive then the predictability horizon is given by [56]

$$t_{\text{horizon}} \sim O\left(\frac{1}{\lambda} \ln \frac{a}{\|\delta_o\|}\right) \tag{20}$$

where a represents an acceptable accuracy with respect to the true trajectory $x(t)$, and $a > \|\delta_o\|$. The logarithmic dependence on $\|\delta_o\|$ defeats any hope of long term system predictability. For example suppose an acceptable accuracy in the model prediction is 10% ($a = 10^{-1}$) and the precision in the initial conditions is $\|\delta_o\| = 10^{-3}$. From Eq. 20, $t_{\text{horizon}} \approx 2(\ln 10)/\lambda$. If the precision in the initial conditions is increased to 10^{-6} then $t_{\text{horizon}} \approx 5(\ln 10)/\lambda$. Increasing the precision in the initial conditions by three orders of magnitude only increases the predictability horizon by a factor of 2.5. For linear systems the predictability horizon is infinite. For stochastic systems (nondeterministic) the predictability horizon is zero.

Chaotic behavior is quite prevalent in mechanical systems that undergo intermittent contact-impact and stick-slip [19]. Beyond the predictability horizon it is more appropriate to describe the dynamic system behavior using statistical theory even though the governing equations are completely deterministic. Furthermore, in this regime, more general notions of convergence are necessary, ones based on statistical theory and measure theory [38]. Certain quantities of interest may be more predictable than others. Global quantities such as dissipated energy, depth of penetration, and the ballistic limit are expected to be more predictable than local quantities such as fracture paths.

7.2 Fracture state space

As the example in Sect. 6 demonstrated, due to the extensive interactions among advancing cracks and ubiquitous self contact-impact, pervasive fracture problems are extremely sensitive to initial conditions. Thus, they exhibit a finite predictability horizon. In an attempt to quantify this predictability horizon for pervasive fracture, consider a given RCP Voronoi mesh with N internal faces. At a high level of abstraction the fracture state of a given face may be described as either uncracked (0) or cracked (1). If the set of all faces is enumerated from 1 to N, the fracture state of the entire body is described by the sequence $(a_1, a_2, \ldots, a_N)$ where each a_i is either 0 or 1. The set of all such binary sequences forms a fracture state space denoted by E^h. Now let X_n represent a crack state at a given time t_n in an explicit dynamics simulation. The sequence $(X_n)_{n\geq 0}$, defines the fracture history. Many other fracture state spaces could be defined as well. If the fracture state is described by the sequence $(c_1, c_2, \ldots, c_N)$ where each c_i is the crack face opening displacement (cfod) of face i, the set of all such sequences forms a new fracture state space denoted by F^h.

A metric space [34] is a set M and a distance function d defined on M such that for all $x, y, z \in M$ the following four axioms hold: (1) d is real valued, finite, and nonnegative, (2) $d(x, y) = 0$ if and only if $x = y$, (3) $d(x, y) = d(y, x)$, and (4) $d(x, y) \leq d(x, z) + d(z, y)$. For the fracture state space E^h one possible distance function is the Hamming distance [23] used in coding and information theory. In this case the Hamming distance function $d_H(x, y)$, $x, y \in E^h$ is defined as the number of faces that have different fracture states (0 or 1). With this metric the distance between two fracture states can be calculated either at different times during one simulation or between two distinct simulations using a specific RCP Voronoi mesh. The Hamming distance between a fracture state at time t_n and the initial fracture state t_0 is a monotonically increasing function of time. For the fracture state space F^h, one possible distance function is the sum of the absolute difference between the crack face opening displacements at two states, X and Y

$$d_{\text{cfod}}(X, Y) = \sum_{i=1}^{N} |\text{cfod}(x_i) - \text{cfod}(y_i)| \tag{21}$$

where the sum is over all faces. Unlike the distance function d_H in the metric space E^h, the distance function d_{cfod} is not necessarily a monotonically increasing function in time due to crack closure.

For an example consider the impact of a concrete beam by a rigid projectile with a striking velocity of 20.0 m/s. The length of the beam is 4.0 m and the thickness is 0.3 m. The RCP Voronoi mesh has a characteristic length of 12 mm with a total of approximately 6,000 elements and 16,000 internal edges. The results of the simulation are shown at the top of Fig. 21 at a simulation time of 3.0 ms. The remaining six cases are simulations using the same mesh and material parameters but with increasingly accurate values of the striking velocity from 20.1 m/s (a difference of 0.5% from the reference value) down to 20.000001 m/s (a difference of 5×10^{-6}% from the reference value). Only in the last two cases are the outer structural cracks visually identical. The distance function d_H can be used to quantify the differences in the crack states. Figure 22 gives the distance between each crack state and the reference as a function of the explicit dynamic simulation step. The last time step shown (6,400) corresponds to the simulation time of 3.0 ms used in Fig. 21. In all cases the distance diverges exponentially (as described by Eq. 19) and then saturates. An accuracy of 5×10^{-9}% in the initial striking velocity is needed to achieve an identical final crack state.

8 Summary

A pure Lagrangian computational method based on randomly close-packed Voronoi tessellations and dynamic mesh connectivity was proposed as a rational approach for simulating the pervasive fracture of materials and structures. Each Voronoi cell was formulated as a finite element using the Reproducing Kernel Method. The randomly seeded Voronoi cells provide a regularized random network of facets for representing cracks. Examples were given of a concrete column impacting a rigid wall and a rigid sphere impacting a concrete beam. It was demonstrated that the fracture patterns and fragmentation statistics are extremely sensitive to initial conditions and display a form of transient chaos. The primary challenge for this class of problems is the definition and demonstration of convergence with mesh refinement for engineering quantities of interest.

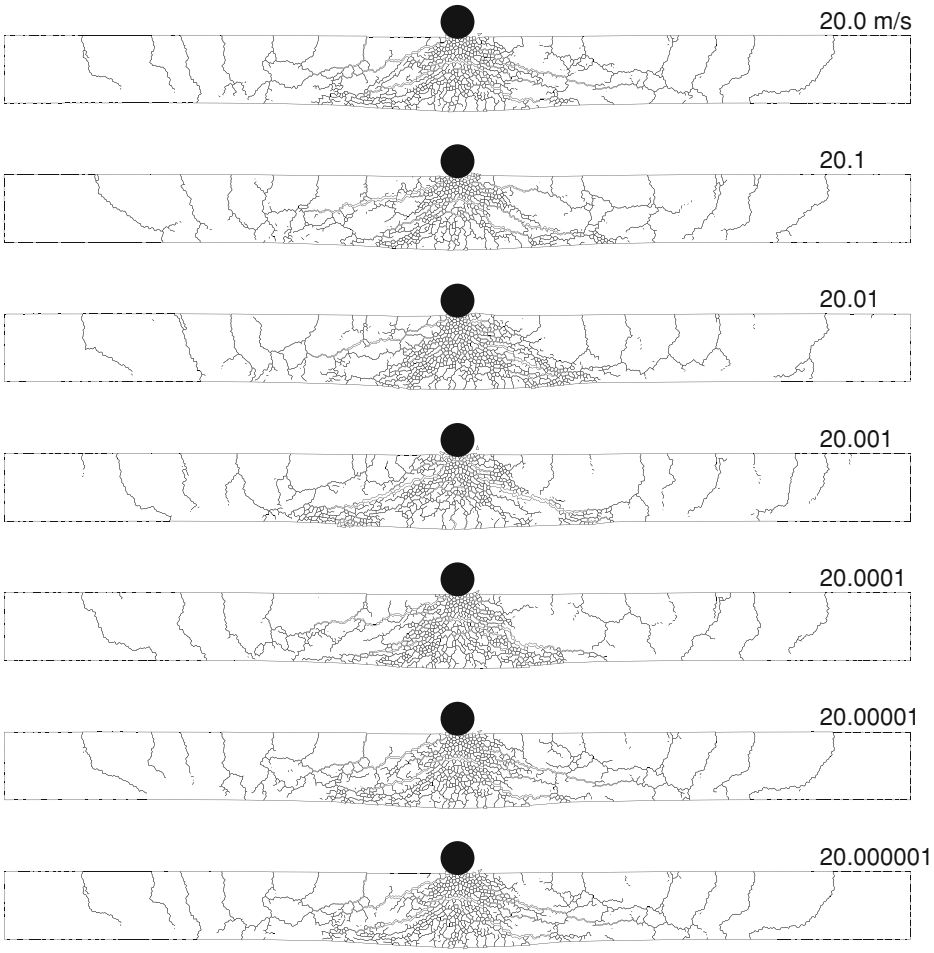

Fig. 21 Crack states resulting from a rigid projectile impacting a concrete column. Each image represents the results from a different simulation with a slightly different striking velocity using the same RCP Voronoi mesh. The simulation time is 3.0 ms after impact which corresponds to the final simulation step (6,400) reported in Fig. 22

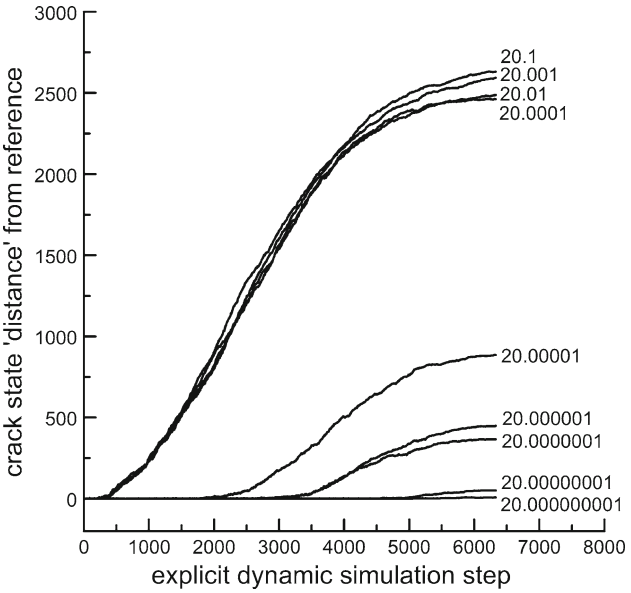

Fig. 22 Distance between crack states resulting from a rigid projectile impacting a concrete column (see Fig. 21) as a function of simulation step. Each curve represents a different simulation with a slightly different striking velocity using the same RCP Voronoi mesh. Distances are with respect to the reference simulation shown at the top of Fig. 21 (striking velocity = 20.0 m/s). The final simulation step (6,400) corresponds to the time of 3.0 ms used in Fig. 21

Acknowledgments The many discussions concerning polyhedral element formulations with Professor Mark Rashid at the University of Califorina at Davis are gratefully acknowledged. Also, the comments and suggestions from the anonymous reviewers were particularly constructive in improving the quality of the paper.

References

1. Aste R, Weaire D (2000) The pursuit of perfect packing. Institute of Physics Publishing, Bristol
2. Attaway S, Heinstein M, Swegle J (1994) Coupling of smooth particle hydrodynamics with the finite element method. Nuclear Eng Design 150:199–205
3. Bazant Z (2005) Scaling of structural strength. Elsevier, Amsterdam
4. Bazant Z, Planas J (1997) Fracture and size effect in concrete and other quasibrittle materials. CRC Press, Boca Raton
5. Belytschko T, Black T (1999) Elastic crack growth in finite elements with minimal remeshing. Int J Numer Methods Eng 45:601–620
6. Belytschko T, Krongauz Y, Organ D, Flemin M, Krysl P (1996) Meshless methods: an overview and recent developments. Comput Methods Appl Mech Eng 139:3–47
7. Belytschko T, Krysl P, Krongauz Y (1997) A three-dimensional explicit element-free Galerkin method. Int J Numer Methods Fluids 24:1253–1270
8. Belytschko T, Liu WK, Moran B (2000) Nonlinear finite elements for continua and structures, Ch. 4.7. Wiley, London
9. Belytschko T, Liu WK, Moran B (2000) Nonlinear finite elements for continua and structures, Ch. 6.2. Wiley, London
10. Bolander J, Saito S (1998) Fracture analyses using spring networks with random geometry. Eng Fract Mech 61:569–591
11. Bolander J, Sukumar N (2005) Irregular lattice model for quasi-static crack propagation. Phys Rev B 71, 094106-1:12
12. Bowyer A (1981) Computing dirichlet tessellations. Comput J 2:162–166
13. Camacho G, Ortiz M (1996) Computational modeling of impact damage in brittle materials. Int J Solids Struct 33:2899–2938
14. Carpinteri A, Chiaia B, Invernizzi S (1999) Three-Dimensional fractal analysis of concrete fracture at the meso-level. Theor Appl Fract Mech 31:163–172
15. Carpinteri A, Pugno N (2005) Fractal fragmentation theory for size effects of Quasi-Brittle materials in compression. Mag Concr Res 57:309–313
16. Chen J, Wu C, Yoon S, You Y (2001) A stabalized conforming nodal integration for Galerkin mesh-free methods. Int J Numer Methods Eng 50:435–466
17. Cusatis G, Cedolin L (2007) Two-scale study of concrete fracturing behavior. Eng Fract Mech 74:3–17
18. Dai K, Liu G, Nguyen T (2007) An n-sided polygonal smoothed finite element method (nSFEM) for solid mechanics. Finite Elem Anal Des 43:847–860
19. di Bernardo M, Budd C, Champneys A, Kowalczyk P (2008) Piecewise-smooth dynamical systems: theory and applications. Springer, Berlin
20. Finney J (1970) Random packings and the structure of simple liquids. I. The geometry of random close packing. In: Proceedings of the royal society of London. Series A, Mathematical and Physical Sciences, vol 319, pp 479–493
21. Gallian J (1994) Contemporary abstract algebra, 3rd edn. D.C Heath and Company
22. Ghosh S, Moorthy S (2004) Three dimensional Voronoi cell finite element model for microstructures with ellipsoidal heterogeneities. Comput Mech 34:510–531
23. Hamming R. (1950) Error detecting and error correcting codes. Bell Syst Tech J 26:147–160
24. Heinstein M, Mello F, Attaway S, Laurson T (2000) Contact-impact modeling in explicit transient dynamics. Comput Methods Appl Mech Eng 187:621–640
25. Hinton E, Rock T, Zienkiewicz O (1976) A note on mass lumping and related processes in the finite element method. Earthq Eng Struct Dyn 4:245–249
26. Hornbogen E (1989) Fractals in microstructure of metals. Int Mater Rev 34:277–296
27. Hu C, Ghosh S (2008) Locally enhanced Voronoi cell finite element model (LE-VCFEM) for simulating evolving fracture in ductile microstructures containing inclusions. Int J Numer Methods Eng 76:1955–1992
28. Hughes T (1987) The finite element method: linear static and dynamic finite element analysis, Ch. 4.4. Prentice-Hall, Englewood Cliffs
29. Hughes T (1987) The finite element method: linear static and dynamic finite element analysis, Ch. 4.5. Prentice-Hall, Englewood Cliffs
30. Hughes T (1987) The finite element method: linear static and dynamic finite element analysis, Ch. 7.3.2. Prentice-Hall, Englewood Cliffs
31. Idelsohn S, Onate E, Calvo N, Pin F (2003) The meshless finite element method. Int J Numer Methods Eng 58:893–912
32. Johnson G, Beissel S, Stryk R (2002) An improved generalized particle algorithm that includes boundaries and interfaces. Int J Numer Methods Eng 53:875–904
33. Josuttis N (1999) The C++ standard library: a tutorial and reference. Addison-Wesley, Reading
34. Kreyszig E (1989) Introductory functional analysis with applications, Ch. 1. Wiley, London
35. Kythe P (1995) An introduction to boundary element methods. CRC Press, Boca Raton

36. Li S, Ghosh S (2006) Multiple cohesive crack growth in brittle materials by the extended Voronoi cell finite element model. Int J Fract 141:373–393
37. Li S, Ghosh S (2006) Extended Voronoi cell finite element model for multiple cohesive crack propagation in brittle materials. Int J Numer Methods Eng 65:1028–1067
38. Lindgren B (1976) Statistical theory, 3rd edn., Ch. 2.5. Macmillan Publishing Co., New York
39. Liu W, Jun S, Zhang Y (1995) Reproducing kernel particle methods. Int J Numer Methods Eng 20:1081–1106
40. Lowen H (2000) Fun with hard spheres. In: Mecke K, Stoyan D (eds) Statistical physics and spatial statistics. The art of analyzing spatial structures and pattern formation. Springer lecture notes in physics, vol 554, pp 295–331
41. Mohammadi S (2003) Discontinuum mechanics: using discrete and finite elements. WIT Press, Billerica
42. Molinari J, Gazonas G, Raghupathy R, Rusinek A, Zhou F (2007) The cohesive element approach to dynamic fragmentation: the question of energy convergence. Int J Numer Methods Eng 69:484–503
43. Okabe A, Boots B, Sugihara K, Chiu S (2000) Spatial tessellations: concepts and applications of Voronoi diagrams. Wiley, London
44. Ortiz M, Pandolfi A (1999) Finite-Deformation irreversible cohesive elements for three-dimensional crack-propagation analysis. Int J Numer Methods Eng 44:1267–1282
45. Pandolfi A, Krysl P, Ortiz M (1999) Finite element simulation of ring expansion and fragmentation: the capturing of length and time scales through cohesive models of fracture. Int J Fract 95:279–297
46. Pandolfi A, Ortiz M (2002) An efficient adaptive procedure for three-dimensional fragmentation simulations. Eng Comput 18:148–159
47. Park Y, Fahrenthold E (2005) A Kernel free Particle-Finite element method for hypervelocity impact simulation. Int J Numer Methods Eng 63:737–759
48. Perfect E (1997) Fractal models for the fragmentation of rocks and soils: a review. Eng Geol 48:185–198
49. Planas J, Elices M, Guinea G, Gomez F, Cendon D, Arbilla I (2003) Generalizations and specializations of cohesive crack models. Eng Fract Mech 70:1759–1776
50. Rabczuk T, Belytschko T (2004) Cracking particles: a simplified meshfree method for arbitrary evolving cracks. Int J Numer Methods Eng 61:2316–2343
51. Rashid M, Selimotic M (2006) A three-dimensional finite element method with arbitrary polyhedral elements. Int J Numer Methods Eng 67:226–252
52. Ruiz G, Ortiz M, Pandolfi A (2000) Three-Dimensional finite-element simulation of the dynamic brazilian test on concrete cylinders. Int J Numer Methods Eng 48:963–994
53. Ruiz G, Pandolfi A, Ortiz M (2001) Three-Dimensional cohesive modeling of dynamic mixed-mode fracture. Int J Numer Methods Eng 52:97–120
54. Schuster H, Just W (2005) Deterministic chaos, an introduction, 4th edn. Wiley-VCH, New York
55. Silling S, Askari E (2005) A meshfree method based on the peridynamic model of solid mechanics. Comput Struct 83:1526–1535
56. Strogatz S (1994) Nonlinear dynamics and chaos with applications to physics, biology, chemistry, and engineering, Ch. 9. Westview Press, Boulder
57. Strouboulis T, Copps K, Babuska I (2000) The generalized finite element method: an example of its implementation and illustration of its performance. Int J Numer Methods Eng 47:1401–1417
58. Sukumar N, Tabarraei A (2004) Conforming polygonal finite elements. Int J Numer Methods Eng 61:2045–2066
59. Sulsky D, Schreyer L (2004) MPM simulation of dynamic material failure with a decohesion constitutive model. Eur J Mech A/Solids 23:423–445
60. Wachspress E (1975) A rational finite element basis. Academic Press, London
61. Watson D (1981) Computing the n-Dimensional tessellation with application to Voronoi polytopes. Comput J 2:167–172
62. Yip M, Li Z, Liao B, Bolander J (2006) Irregular lattice models of fracture of multiphase particulate materials. Int J Fract 140:113–124
63. Yip M, Mohle J, Bolander J (2005) Automated modeling of three-dimensional structural components using irregular lattices. Comput Aided Civil Infrastructure Eng 20:393–407
64. Zallen R (2004) The physics of amorphous solids, Ch. 2. Wiley-VCH, New York